ACES Asian Chemical Editorial Society

doi.org/10.1002/cnma.202100428

CHEMNANOMAT
Research Article

www.chemnanomat.org

Synthesis and Characterization of a Carbon-Supported Cobalt Nitride Nano-Catalyst

Anosha Rubab,[d] Nadeem Baig,[b] Muhammad Sher,[c] Mubarak Ali,*[a] Anwar Ul-Hamid,[e] Naila Jabeen,[f] Latif U. Khan,[g] and Manzar Sohail*[d]

Abstract: Transition metal nitrides have attracted great interest among the non-noble catalysts employed in heterogeneous catalytic processes because of their exceptional stability and catalytic potential. However, the approach for their synthesis has remained a tremendous challenge. This study presents the synthesis of Co_4N/C catalyst fabricated at 400, 600, and 800 °, symbolized as Co_4N/C-400, Co_4N/C-600, Co_4N/C-800, respectively. The characterization of fabricated catalysts is carried out through various advanced analytical techniques. As prepared nano-catalyst Co_4N/C shows remarkable catalytic efficiency in terms of low activation energy ($E_a = 3.038 \times 10^{-1}$ KJ mol^{-1}), fast conversion rate ($K_{app} =$ 0.2884 s^{-1}), and 97.57% conversion efficiency. Moreover, it also exhibits excellent stability and reusability because of its metallic characteristics. The outstanding catalytic activity of the catalyst is the combined effect in which the Co_4N nanoparticles acted as active sites, and the carbon support doped with nitrogen provided an expressway for the transport of electrons required for catalytic reduction. Moreover, the designed catalyst is immobilized on the cellulose membrane filter support, to demonstrate the catalytic reduction of 4-nitrophenol to 4-aminophenol. We envision that our work would facilitate the fabrication of cobalt nitrides-based nano-catalysts for a wide range of industrial applications.

1. Introduction

Nitrides are an attractive class of interstitial compounds because of their remarkable physical and chemical properties, which allow them to be employed in a wide range of technological and industrial applications. The properties of metal nitrides, particularly transition metal nitrides (TMNs), can be tuned for a range of applications.[1] Metal nitrides have been employed in the field of hard coatings for storage devices and cutting tools[2] due to their distinctive mechanical properties, hardness, brittleness, corrosion resistance,[3] and high thermal stability.[1] The unique bonding parameters in nitrides result in a unique electronic structures that can be tuned to achieve the metallic to semiconducting materials,[4] which are of great significance in electronics,[5] optoelectronics,[6] ceramics,[7] supercapacitor electrodes,[8] magnetic materials,[9] photovoltaics,[4] refractories[5,10] sensors[11] and spintronics.[12] In contrast to oxides, nitrides cannot readily sinter due to their high lattice energies resulting in small particle size without impeding the crystallite size.[13] TMNs have received considerable attention in catalysis as catalysts, photocatalysts, and electrocatalysts with the great potential to substitute noble metals, oxides, and sulfides. In addition, nitrides have also been employed as support material to enhance the catalytic activity of precious metals like Pt and Pd, besides being used as active species for catalysis.[14] These unique physicochemical properties of MNs can be attributed to the subsequent participation of ionic, covalent, and metallic bonding.[15] The crystal structure and geometry of TMNs is such that the inclusion of nitrogen to the host metal modifies its electronic structure because of the charge transfer processes and structural modification, owing to the expansion of the metal-metal lattice parameter.[15–16] Metal

[a] Dr. M. Ali
Materials Research Department, GSI Helmholtzzentrum für Schwerionenforschung
Planckstrasse 1, D-64291, Darmstadt (Germany)
and
Fachbereich Material- und Geowissenschaften, Fachgebiet Materialanalytik
Technische Universität Darmstadt
Alarich-Weiss-Str. 2, D-64287 Darmstadt (Germany)
E-mail: M.Ali@gsi.de

[b] Dr. N. Baig
Interdisciplinary Research Center for Membranes and Water Security
King Fahd University of Petroleum and Minerals
Dhahran 31261 (Saudi Arabia)

[c] Dr. M. Sher
Department of Chemistry
Allama Iqbal Open University
Islamabad 44000 (Pakistan)

[d] A. Rubab, Prof. Dr. M. Sohail
Department of Chemistry, School of Natural Sciences
National University of Sciences and Technology
Islamabad 44000 (Pakistan)
E-mail: Manzar.sohail@sns.nust.edu.pk

[e] Dr. A. Ul-Hamid
Core Research Facilities,
King Fahd University of Petroleum and Minerals
Dhahran 31261 (Saudi Arabia)

[f] Dr. N. Jabeen
Nanosciences and Technology Division
National Centre for Physics, QAU Campus
Shahdra Valley Road, P.O. Box 2141, Islamabad 44000 (Pakistan)

[g] Dr. L. U. Khan
Synchrotron-Light for Experimental Science and Applications in the Middle East (SESAME)
P.O. Box 7, Allan 19252 (Jordan)

Supporting information for this article is available on the WWW under https://doi.org/10.1002/cnma.202100428

atoms occupy the lattices of crystal structures, while the nitrogen atom takes the interstitial sites between the metal sublattice. Geometric and electronic parameters govern the crystal structure of MNs. MNs obey Hägg rule (less than 0.59 ratio of radii of nonmetal to metal gives rise to simple structures) owing to the small size of nitrogen (0.065 nm).[17] The bonding in TMNs results from the hybridization of d-orbital (e_g and t_{2g}) of metal and s-p orbitals of a nonmetal is considered responsible for a wide range of properties.[18] In crafting the analogies among noble metals, oxides, and nitrides for catalysis, MNs present distinct properties, and chemistry making them a potential candidate for catalysis.[16]

Recently, substantial interest has been observed in nitrogen-based catalysts since the successful synthesis of new carbon nanostructures with the increased electron density near the Fermi level due to the contraction of d-band and the enhanced adsorption of reactants.[16] Hence, it is highly desirable to synthesize and explore the catalytic activity of metal nitrides because of their great potential to supersede noble metals. TMNs, besides having a large surface-to-volume ratio, also offer size and shape selectivity for catalysis.[13] TMNs have been reported to show excellent catalytic activity for reactions entailing hydrogen treatment like hydrogenation, dehydrogenation, hydrodesulfurization,[19] hydrodenitrogenation, hydrogenolysis, CO hydrogenation, alkane isomerization, and hydride activation.[13,20] Binary and ternary TMNs (Mo_2N, VN, W_2N, and Co_3Mo_3N) have proven efficient catalysts for ammonia synthesis compared to commercial iron and noble ruthenium catalysts.[21] Furthermore, the corrosion resistance, electrical conductivity, and mechanical stability make nitride-based electrocatalysts proficient in being a promising alternative for Pt electrocatalysts for hydrogen evolution reaction (HER), thus minimizing the increased cost and scarcity of noble metal-based materials.[22] Moreover, Ni_3N nanosheets,[23] Co_4N nanowires,[24] and ternary nitrides (Ni–Co, Co–Fe, and NiFe)[25] have shown extraordinary oxygen evolution reaction (OER) and oxygen reduction reaction (ORR) performance with low overpotential and long-term stability.

Even though nitrides outperform noble metals, oxides, and sulphides in various applications, yet they have not been explored to a great extent at their potential because of the challenging requirements for the synthesis of nitride materials. Synthetic approaches employed for nitrides can be classified into physical and chemical routes. Physical approaches for synthesis include physical vapor deposition (PVD), laser, and arc plasma methods. These methods, however, can produce a limited variety of nitrides, such as CrN and TiN.[15] Contrary to Physical methods, chemical methods are effective which involve nitridation of precursor metal powders, metal oxides, or sulfides by N_2, NH_3, hydrazine and urea at high temperature and pressure. The product obtained through these high temperature and pressure programmed reactions may have large particle size and metallic impurities.[5,26] Another route for the synthesis of TMNs is mechanochemical ball milling. This method continuously exposes new metal surfaces due to ball milling of metal powder under N_2 or NH_3 flow. The drawbacks of this method are the long time for process completion, Fe impurities introduction during the process, and the requirement of the post-annealing and high-pressure conditions.[13] Another commonly used approach is solid-state metathesis which involves large activation energies to control the diffusion barrier. The reaction is carried out by grinding the alkali or alkaline earth nitrides and metal halides at room temperature, then heating in a furnace. Due to the short reaction time, pure phase nitrides are not obtained through this method.

The solvothermal method using solvents above their boiling points in an autoclave is widely applicable for synthesizing TMNs. It requires moderate temperature conditions and the liberty to control the size and shape of metal nanoparticles. Metal nanoparticles obtained through this route are agglomerated, sometimes requiring post reaction annealing and a capping agent to the reaction system.[27] MN phases of Zr^{4+}, Nb^{5+}, Ga^{3+}, In^{3+}, and Ti^{4+} have been reported by decomposing their respective dialkylamides with liquid NH_3. The likelihood of formation of structural motifs before crystallization can give rise to different phases of obtained product.[28] The sol-gel method has also been applied to synthesize porous nitride nanostructures. This process is carried out at low temperatures. Thus, there is an opportunity to control the size of nanostructures. However, the sol-gel process's precursors are sensitive to oxidation and not cost effective.[13] Ken Niwa et al. used a high-pressure technique to fabricate iron and cobalt nitrides by employing a diamond anvil cell onto which transition metal foil was placed along with nitrogen loading, which was succeeded by irradiating with infrared laser under high pressure.[29]

Despite all efforts and adopting energy-intensive, costly, and extensive procedures for synthesizing TMNs, obtaining pure phase is still a challenge, i.e., some oxide phases are also produced along with TMNs. Recently, metal-organic frameworks (MOFs) have been employed as sacrificial templates to synthesize high surface area nanostructured metal and metal oxides. Annealing or acid leaching of MOFs under optimized conditions results in highly disperse and well-controlled nanostructures. Linker in MOFs provides linkage sites to metal ions through coordination bonds which provide porosity to the matrix. Oxygenated linkers offer oxygen donor as linkage site whereas nitrogen in the linker favor well dispersed M–N species.[30] Single source metal precursors allow the stoichiometry of the precursors to remain the same, creating a feasible pathway to produce nanomaterials in a pure phase.

Single source metal precursors are the practical and clean route for synthesizing nanocomposites, and these precursors are receiving significant attention in the synthesis of pure nanomaterials.[31,32] Herein, we have employed a facile approach to synthesize pure cobalt nitride by using single-source metal precursors. The ligands are rationally selected, containing only nitrogen as a donor atom to avoid the unwanted impurities in the nanostructured material. Cobalt chloride hexahydrate ($CoCl_2 \cdot 6H_2O$) was used as a metal precursor. Hexamethylenetetramine was employed as a coordinating ligand and 7,7,8,8-Tetracyanoquinodimethane (TCNQ) anion as an anionic linker to convert simple complexes into coordination polymers. $TCNQH_2$, the reduced form of TCNQ is a suitable source for

various types of $TCNQ^{-2}$-based coordination polymers.[33] Annealing of as-synthesized coordination polymer under N_2 flow at 400,600 and 800 °C was carried out to obtain metal nitride. Annealing of coordination polymer at 800 °C resulted in pure phase Co_4N. Considering the excellent magnetic properties and high surface area of Co_4N, it was tested for the selective reduction of 4-Nitrophenol to 4-Aminophenol as a model reaction. $NaBH_4$ was used as a reductant and hydrogen source for the reaction.

2. Results and Discussions

FTIR Analysis

The coordination of a polynitirile TCNQ to a metal ion, charge transfer steps, structural properties, and intermediate coordination affects the strength of chemical bonds forming the polymeric complex, which can be explained by the vibrational frequencies of TCNQ. Nitrile stretching vibration in TCNQ has indicated the charge transfer as it is shifted from 2222 cm^{-1} to 2130 cm^{-1}. It provides an insight that TCNQ is present as a dianion ($TCNQ^{-2}$) and is in conjugation and coordination with Co(II).[34] A vibrational stretch of C=C neutral TCNQ at 1542 cm^{-1} is shifted towards a lower frequency at 1504 cm^{-1} after interaction with the Co(II).[35] A sharp peak at 1601 cm^{-1} illustrates the stretching vibration of the benzene ring. A small peak at 1654 cm^{-1} can be ascribed to singular and conjugated C=C stretching vibrations.[36] The bands at 1460 cm^{-1}, 1377 cm^{-1}, and 1226 cm^{-1} can be assigned to CH_2 bending, wagging, and scissoring vibration, respectively associated with HMTA ligand.[37] C–N stretching peaks at 1189 cm^{-1} and 1020 cm^{-1} can be attributed to polynitirile molecule and N–H stretch. C–N stretching peaks of HMTA at 812 cm^{-1} shift to higher frequency at 821 cm^{-1}, showing the coordination of HMTA to Co(II).[38] Besides, around 685 cm^{-1} a bending vibration of N–C-N can be observed. Lastly, a characteristic Co–N band appears in low frequency region 563 cm^{-1}, which is in accordance with reported literature.[39] The appearance of the various absorbance band and their peak shift of the functional groups has endorsed the successful formation of coordination polymer (Figure 1).

Upon annealing of coordination polymer, reduction in peaks is observed, which can be reflected in FTIR spectra. Spectral signatures of C–C, C–N, and C–H have significantly been removed in the structure, suggesting the dissociation of ligands and nitride formation. However, a characteristic peak of Co–N retains as in coordination polymer, indicating metal nanoparticles supported on carbon matrix in an annealed sample.

Raman Spectroscopy

Raman scattering studies illustrate a graphene-like structure of carbon support. Raman spectrum of Co_4N/C-800 exhibits a peak at 1500 cm^{-1}, which is characteristic G-band, and a sharp peak at 2800 cm^{-1} can be attributed to G′, also called 2D band.[40] Raman studies of Co_4N/C-600 also show peaks around 1500 cm^{-1} and 2800 cm^{-1} but with relatively lower intensity than Co_4N/C-800. The absence of sharp spectral peaks in Co_4N/C-400 indicates the incomplete decomposition of coordination

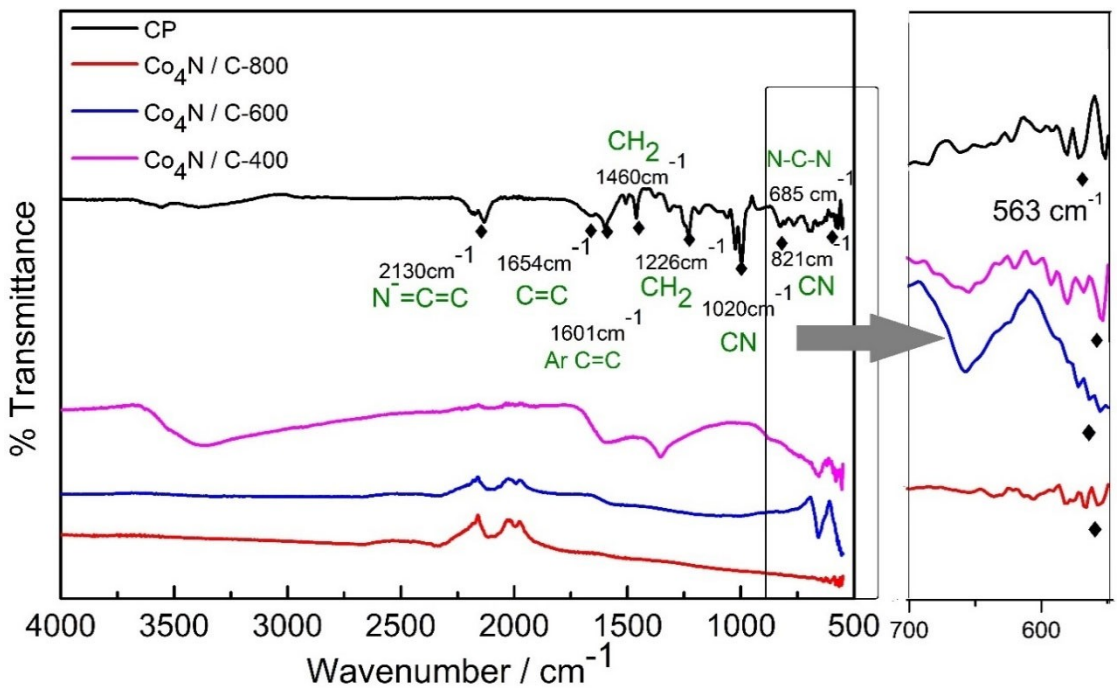

Figure 1. FTIR spectra of cobalt nitride precursor (CP) and Co_4N/C synthesized at 400 (Co_4/C-400), 600 (Co_4N/C-600) and 800 °C (Co_4N/C-800).

polymer, whereas the appearance of a peak at 632 cm^{-1} shows the vibrational mode of elemental cobalt (Figure 2).

pXRD of Coordination Polymer, and calcined products

The powder X-ray diffraction data of coordination polymer recorded at 2θ values ranging from 10–80°. The sharp diffraction peaks were absent, which indicates the amorphous nature of the material. pXRD profiles of nitrated products at 400, 600, and 800 °C were scanned with a scanning step at 0.05°. Coordination polymer annealed at 400 °C is not differentiated into significant peaks. However, the annealing of precursor polymer at 600 °C shows a sharp peak positioned at a 2θ value of 44.2°. Because no other sharp diffraction peaks were observed, the material was further nitrided to 800 °C, resulting in a well-crystallized Co_4N from amorphous coordination polymer (Figure 3). The diffraction peaks at 2θ value of 44.2°, 51.5°, and 76°, correspond to (111), (200), and (220) planes, respectively (JCPDS#41-0943).[41] Theoretical studies about the crystal structure of Co_4N reveal that Co atoms take the (111) plane while N atom occupies the interstitial position of the metal sublattice (space group-*pm-3m (221)*).[42] The Scherrer equation gives 19.30 nm crystallite size for the annealed product at 800 °C. The diffraction pattern of nitridated product at 800 °C shows successful conversion of coordination polymer to pure Co_4N.

Morphological analysis of coordination polymer and Co_4N

The detailed morphology and structural development of Co_4N from coordination polymer were scanned through Scanning Electron Microscopy images (SEM). SEM images of coordination polymer show a uniform amorphous 3D network in the absence of any support shown in Figure 4(a). Nitridation to Co_4N results in uniform growth of Co_4N nanosheets anchored on a carbon support. Annealing results in the porosity of nanosheets and the roughness of the surface. The porosity and the surface roughness might be appeared due to the decomposition and carbonization of HMTA and TCNQ anionic linker.[43] Furthermore, the energy-dispersive X-ray spectroscopy (EDX) in Figure 5 shows an evenly spatial distribution of Co, N in well-defined contact with the C surface. According to the EDX spectrum, the wt.% of Co, N, and C appeared 28.8, 6.3, and 64.9%, respectively. These percentages are indicative that carbon is acting as support on which the Co_4N nanoparticles are well dispersed to perform the catalytic activity.

Transmission elecron microscopy (TEM) analysis of the synthesized nanostructured materials has provided an in-depth analysis of their morphology and crystalline structure. The TEM image of the Co_4N/C has shown that the Co nanoparticles are well dispersed and embedded in porous nano carbon-nitrogen layers giving a crystalline morphology to Co_4N/C (Figure 6). The more pores on the Co_4N/C surface accounts for the enhanced catalytic activity as pores provide additional active sites for adsorption.[44] The crystallite size of cobalt nanoparticles calculated from HR-TEM images is ranged from 17 to 19 nm, which correlates well with XRD analysis. Indexing crystal lattice fringes

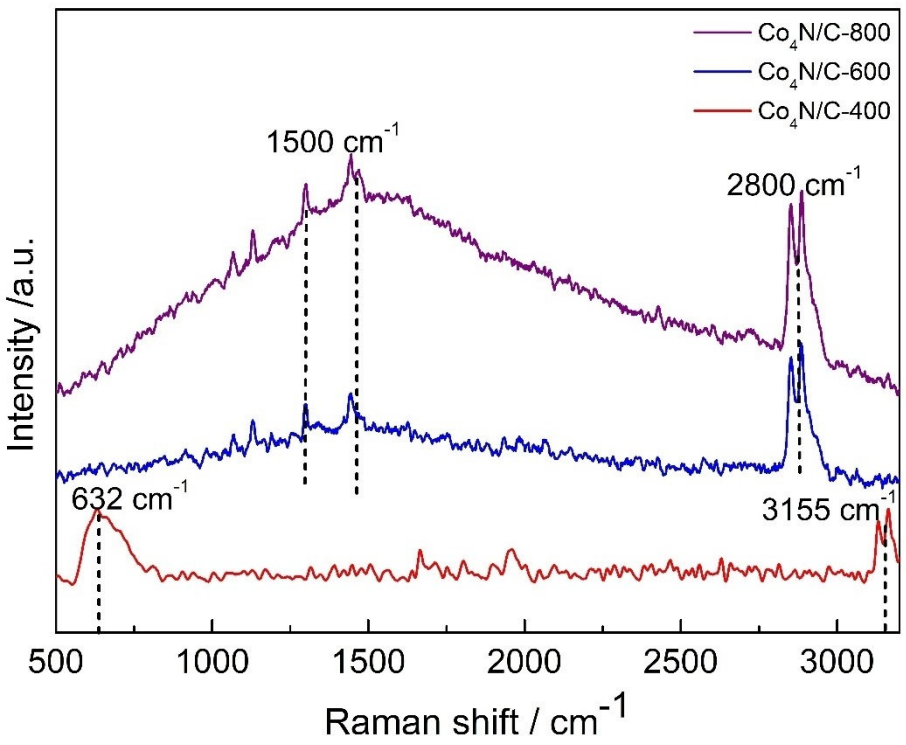

Figure 2. Raman Scattering Spectra of catalysts synthesized at different temperature.

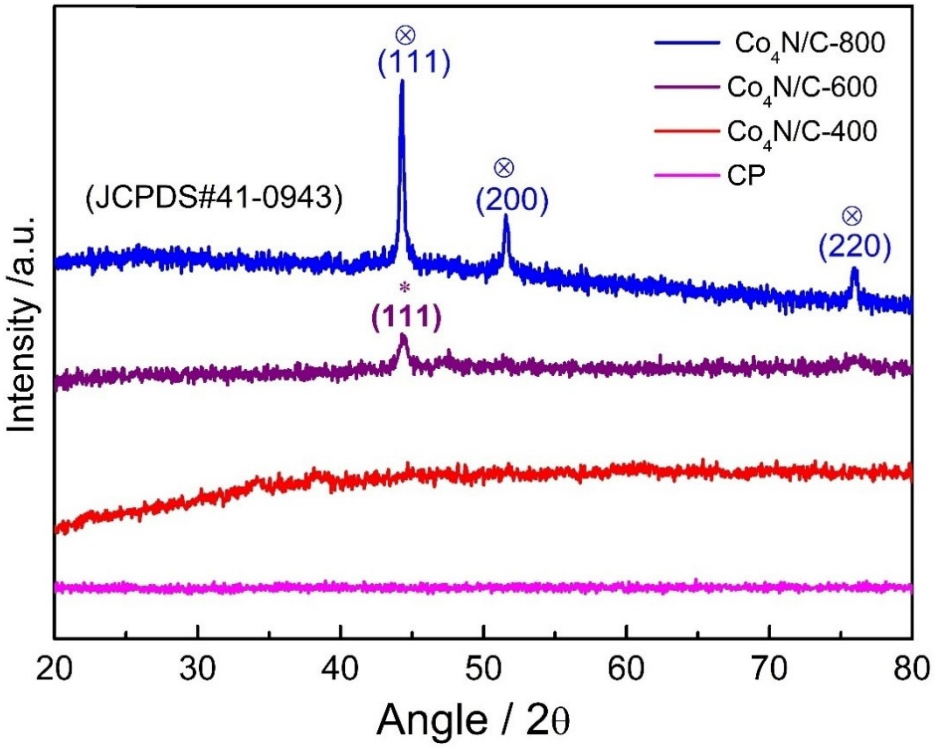

Figure 3. pXRD patterns of Co_4N precursor (CP) and catalysts synthesized at different temperature.

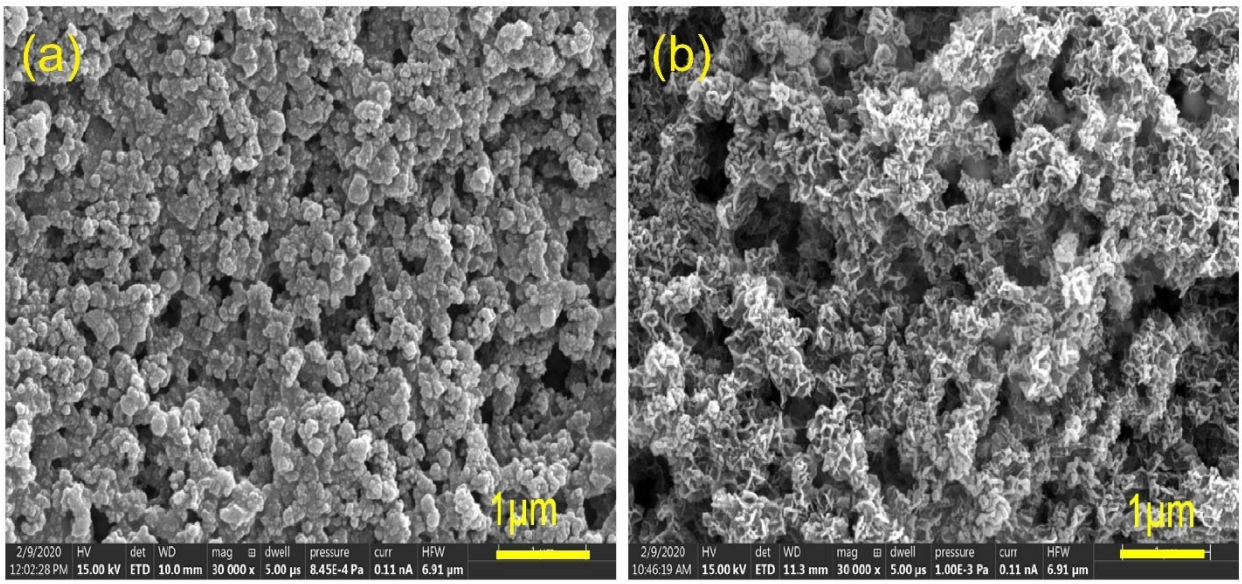

Figure 4. SEM micrographs of (a) Coordination polymer (b) Co_4N/C-800 catalyst at 1 μm resolution.

with an average distance of 0.2033 nm corresponds to the (111) plane of Co_4N, demonstrating the successful conversion to Co_4N/C after nitridation. The 0.3 nm distance between the lattice fringes of carbon layers supports carbon architecture's crystallinity and the uniformly embedded cobalt nanoparticles.[45] In addition, the SAED pattern of as-synthesized Co_4N/C has appeared as bright spots that take the shape of concentric circles, supporting the polycrystallinity of the substance. Interplanar spacing(d_{hkl}) obtained from SAED images is provided the values of 0.20 nm, 0.18 nm, and 0.13 nm, which correlate perfectly with (111), (200) and (220) planes of Co_4N, respectively.[46]

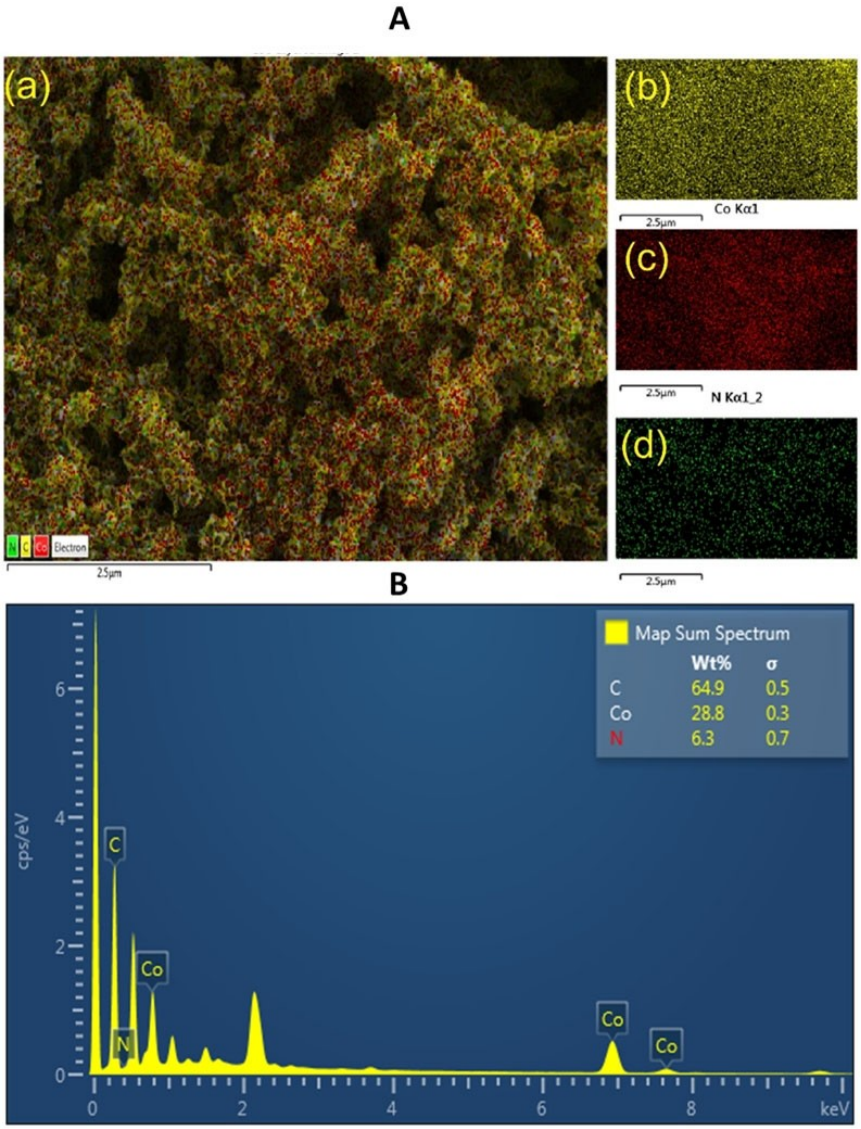

Figure 5. (A) (a) Elemental Mapping of Co_4N/C-800 (b) C (c) Co (d) N elements. (B) Energy-dispersive X-ray spectrum of Co_4N/C-800.

Thermal behavior of coordination polymer and catalysts surface area analysis

To determine the stability and thermal degradation pattern of coordination polymer, thermal gravimetric analysis (TGA) was carried out in an inert atmosphere. The initial loss below 221.58 °C can be attributed to solvent and moisture loss. The weight loss becomes consistent at 676.24 °C, which is due to the loss of carbon, making 76.3% of the total weight loss (Figure 7a).

The surface area of the designed catalyst is critical in determining its efficiency for a particular reaction. The surface areas of the various synthesized catalysts were analyzed through Brunauer Emmet Teller (BET) measurements. The BET surface area of Co_4N/C-800, Co_4N/C-600, and Co_4N/C-400 is found 296.1237 m^2/g, 183.6048 m^2/g, and 108.1872 m^2/g, respectively. The high specific surface area of Co_4N/C-800 has revealed its dispersion and small particle size of Co_4N nanoparticles around crystalline carbon layers. As evident from the BET analysis, SEM/TEM images, the exceptionally high surface area, and better dispersion on the graphitic carbon support have made its potent catalyst with better stability and chemical activity. The existence of hysteresis in the desorption route indicates inter-particle mesoporosity[47] (Figure 7b). The corresponding average pore radius of Co_4N/C-800, Co_4N/C-600, and Co_4N/C-400 are 1.7 nm, 1.7 nm, and 1.8 nm, respectively. The small change in pore radius is consistent with reported studies.[48]

XPS Analysis

For the detailed chemical states and the elemental composition of Co4 N/C-800, X-ray photoelectron spectroscopy (XPS) was

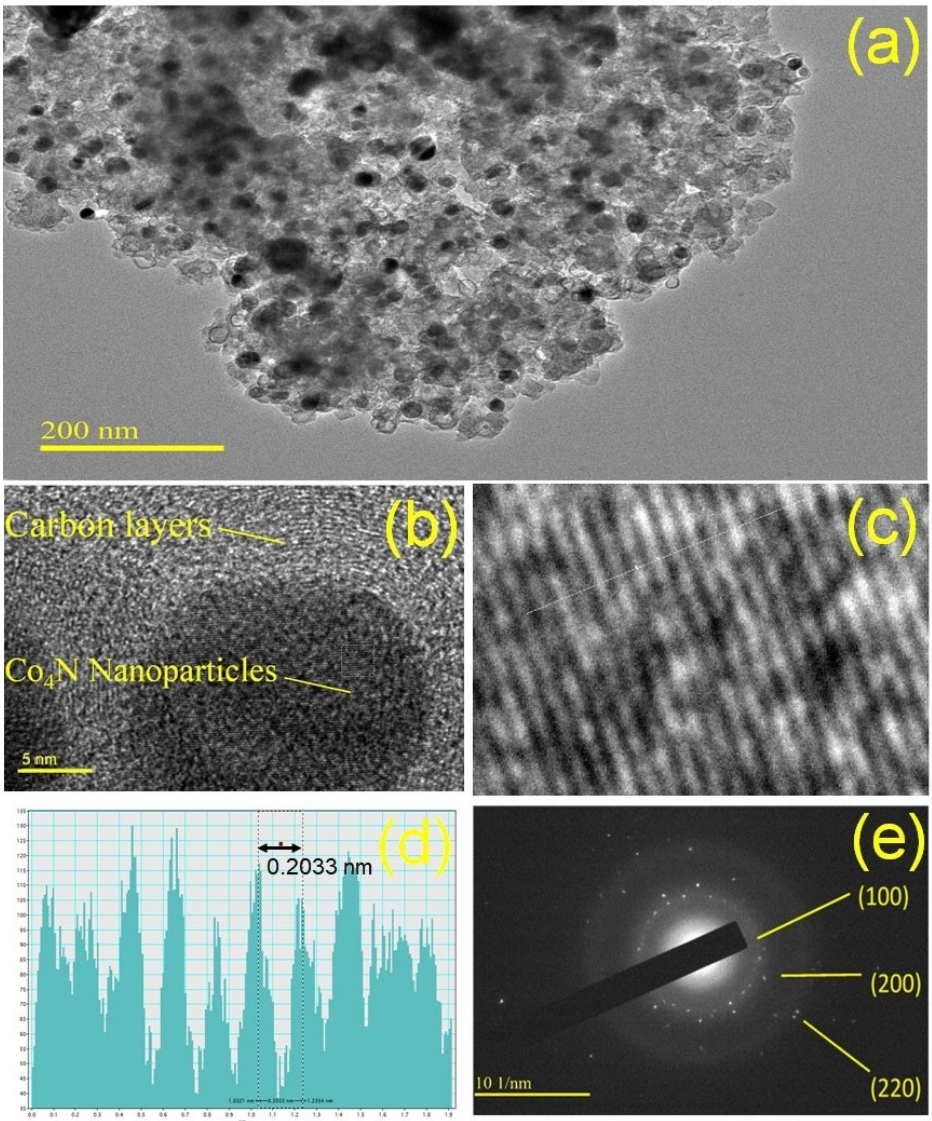

Figure 6. (a) TEM image of Co_4N/C-800 (b) Enlarged image of Co_4N nanoparticles coated with carbon layers (c) Inverse FFT image of a Co_4N/C-800 nanoparticle (d) Profile graph of inverse FFT and FFT of image c (e) SAED pattern of Co_4N/C-800.

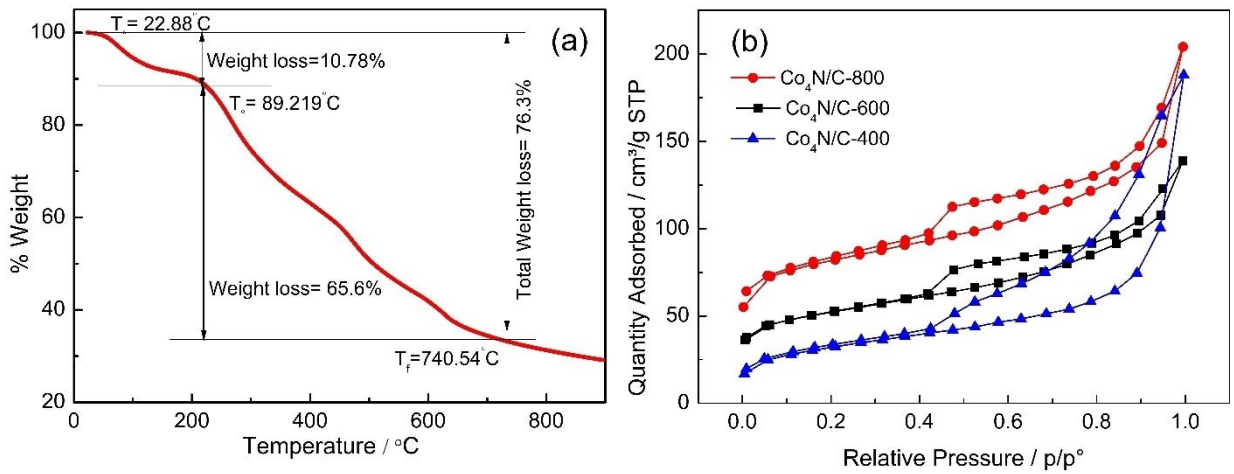

Figure 7. (a) TGA of coordination polymer measured in an inert atmosphere (b) Nitrogen adsorption-desorption isotherms measured at 77 K.

carried out using Al K α source of radiation. The survey spectrum has shown the presence of the constituent elements such as cobalt, carbon, and nitrogen, which has shown the purity of the sample. Although, the less intense oxygen peaks have been observed in the survey spectrum that may have come from the adsorbed moisture from the sample's surface. The high-resolution deconvoluted XPS spectra of Co, C, and N have revealed the detailed information about their chemical states shown in Figure 8. The narrow scan spectrum of Co 2p shows its deconvolution into two $2p_{3/2}$ and $2p_{1/2}$ peaks along with their corresponding satellite peaks. XPS analysis determines oxidation states by differentiating between metallic zerovalent cobalt and the higher oxidation states (Co^{+2}, Co^{+3}). Co 2p narrow scan spectrum shows deconvoluted peaks having binding energy value at 777.3 eV, 779.0 eV, 794 eV, and 802.7 eV. The minor $2p_{3/2}$ peak at 777.3 eV can be ascribed to the Co–Co bond (metallic bond). Major peaks at 779.0 eV and 794.6 eV can be attributed to Co $2p_{3/2}$ and Co $2p_{1/2}$, which are shifted towards higher binding energy than Co (0), which infers that the Co oxidation state is higher than zero. XPS spectrum indicates the existence of higher oxidation state of Co in Co_4N, as the coexistence of Co^{+3} and Co^{+2} can be ascribed to Co_4N.[49] Furthermore, the presence of satellite peaks at 784.7 eV and 802.7 eV indicates an oxidation state higher than zero, as satellite peaks are absent in the metallic Co. As XRD of both metallic Co and Co_4N is not conclusive to differentiate between the two, XPS results show the formation of Co_4N rather than metallic Co.

The deconvoluted peak of N at 398.0 eV indicates the corresponding metal to nitrogen bond. Since nitrogen present at the interstitial sites binds to less electronegative Co atoms, its peak shifts towards lower binding energy. This shift towards lower binding energy is due to electron gain by N atoms at the cost of Co atoms.[50] The prominent peak that appeared at 400.6 eV can be attributed to pyrrolic nitrogen, whereas a broad peak at 401.7 eV might be appeared due to graphitic nitrogen.[51] The pyrrolic nitrogen gives two p electrons to the p system, while the graphitic nitrogen atoms substitute for C atoms present in the ring.[52]

C 1s spectra show a sharp peak at 284.2 eV, suggesting sp^2 hybridized carbon, representative of graphitic layers around Co_4N particles. The prominent peak at 284.9 eV might be due to the amorphous sp^3 hybridized carbon, and a minor peak at 286.8 eV can be accredited to carbon and nitrogen bond. Besides, O 1s peaks were also encountered in the XPS spectrum of Co_4N/C-800 at the binding energy value of 531.6 eV. However, the O 1s peak at 531.6 eV in the XPS spectrum of

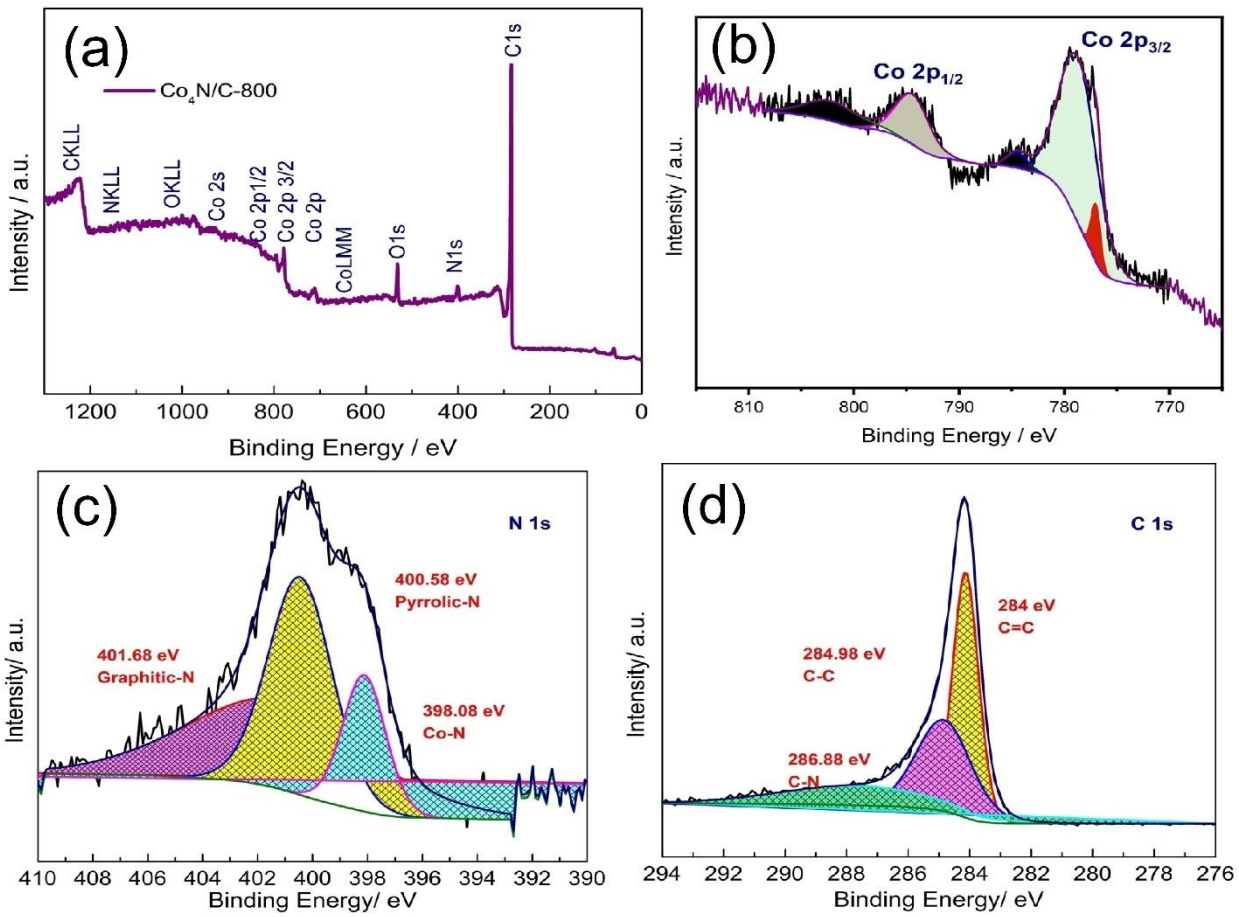

Figure 8. (a) Survey scan XPS spectra of Co_4N/C-800. High-resolution XPS spectra of (b) Co2p, (c) N1s, and (d) C1s.

Co4 N/C-800 is appeared due to adsorbed oxygen species on the sample's surface, which is generally unavoidable.

Local Atomic Structure Investigation by XAFS

The local coordination environment of the Co_4N thin film was explored by conducting the X-ray absorption fine structure (XAFS) characterization. Figure 9a shows the Co K-edge (7709 eV) X-ray absorption near edge structure (XANES) spectra of the Co_4N thin film in comparison with the Co standard foil and rocksalt cubic CoO thin film, which were used as reference materials. The rising absorption edge of Co_4N is located approximately between those of Co and CoO, indicating the average valence of Co should be between the metallic Co and Co^{2+} in CoO lattice. Fourier transform (FT) of the Co K edge (7709 eV) EXAFS spectrum of Co_4N (Figure 9b), displays two typical peaks correspond to the Co–N (~1.3 Å) and Co–Co (~2.4 Å) bonds pairs,[24] when compared to the reference Co standard foil and rocksalt cubic CoO, demonstrating the existence of the Co_4N cubic phase, corroborated through the XRD patterns (Figure 3).

The continuous Cauchy wavelet transform (CCWT) analysis was applied to the k^2-weighted EXAFS data of Co_4N, in order to more clearly detect as colored two-dimensional images the local coordination environment around Co in Co_4N, using a high programing language MATLAB R2020a based code, developed by Muñoz and coworkers in 2003.[53] CCWT modulus is clearly visualized the various coordination shells of the neighboring atoms around the photoabsorber in form of different RGB colored maps in the 2D CCWT image,[54] concurrently analyzing the EXAFS data of the material into respective two-dimensional *k* and *R* spaces. Thus, the CCWT 2D-image of Co_4N thin film (Figure 9d) demonstrated the distinct yellowish green colored map associated with the N back-scatterer in first coordination shell and dark red colored map corresponded to the Co atoms in second coordination shell, by decomposing the EXAFS signal of Co_4N in related k-and R-spaces. It is noteworthy that the yellowish green colored map (Figure 9d) for the N backscatter in first coordination shell of Co_4N was found at lower R (1.3 Å), when compared to the color map for O atomic group (1.65 Å) in the 1st coordination shell of CoO (Figure 9c), closely correlated with the first peak of its Fourier transform of $\chi(k)$, validating the existence of C–N bond pair for the Co_4N. Finally, the color map located at high R (~

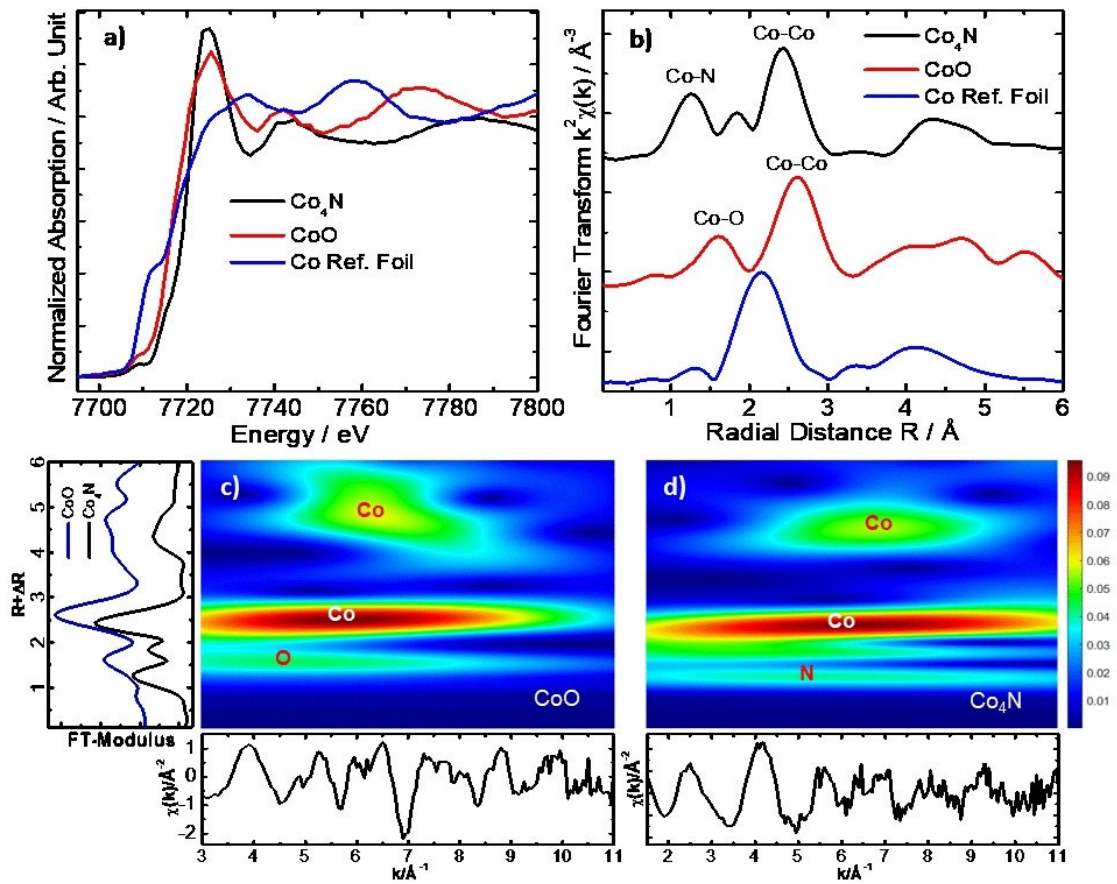

Figure 9. Normalized XANES spectra (a) and Experimental Fourier transforms of k^2-weighted EXAFS signals at the Co *K*-edge (7709 eV) of the Co_4N thin film in comparison with the references, Co standard foil and CoO film (b). Continuous Cauchy wavelet transform analyses of reference CoO (c) and Co_4N thin film (d) EXAFS signals, manifesting the clear localization of N and Co back scatterers contributions in different yellowish green and dark red color maps, respectively for the Co_4N, when compared to the reference CoO.

4.3 Å) represents a higher-order shell, originating from the single backscattering of metal atomic groups (Co) from the other octahedra of Co_4N cubic lattice.

Catalytic reduction of 4-Nitrophenol

The catalyst's efficiency was evaluated against the model catalytic reaction in which 4-nitrophenol converted into 4-aminophenol in the presence of $NaBH_4$ and catalyst.[55] Before catalysis, the absorption peak of pale-yellow solution of 4-NP was recorded at 317 nm. The addition of $NaBH_4$ resulted in the formation of nitrophenolate ions that exhibited the maximum absorption at 400 nm due to increased alkalinity. The intensity of this peak is proportional to the concentration of nitrophenolate ions.[56] The reaction system remained stable for 25 min, and no decrease in absorption intensity of nitrophenolate ions was observed, indicating that the repulsion between BH_4^- and nitrophenolate ions can not cause any reduction. The catalytic evaluation of as prepared Co_4N/C-800 catalyst was determined by its addition to the reaction mixture, which led to the reduction of 4-NP to 4-AP in an extremely short time of 15 s indicated by the instant change in colorless solution from deep yellow 4-NP solution, followed by the appearance of a 4-AP peak at 300 nm (Figure 10). Catalytic loading >2 mg is difficult to handle with UV-Vis adsorption due to fast reaction kinetics which does not provide enough time to record the spectra.

The catalytic performance of Co nanocomposites synthesized at 600 °C and 400 °C, Co (TCNQ)-800 complex, Co (II)-HMTA-800 complex, and coordination polymer were compared by following a similar procedure for reduction. The comparison has shown the reduced catalytic performance because of less availability of active sites. Co_4N/C-600, Co_4N/C-400, Co (TCNQ)-800 complex, and Co (II)-HMTA complex were able to reduce 4-NP to 4-AP in the 20s, 70s, 45 s, and 300 s, respectively. Thus, the Co_4N/C-800, among other synthesized catalysts, has shown the super-efficient catalytic performance for the reduction of 4-NP.

Kinetic Studies

The reaction can be attributed as pseudo-first order with respect to 4-NP. Since in the designed model reaction, the concentration of 4-NP can be viewed as constant throughout the reaction, while $NaBH_4$ concentration is in excess compared to 4-NP and reaction rate independent of NaBH4 concentration. Kinetic studies indicate the conversion of 4-NP by the following relation.

$$\ln\left(C_t/C_o\right) = -K_{app}\,t$$

where C_t and C_o are the concentrations at a given time t and the initial concentration of 4-NP. The catalytic efficiency of Co_4N/C-800, Co_4N/C-600, and Co_4N/C-400 indicated by the plot of C_t/C_o against time in Figure 11a reveals that the catalyst

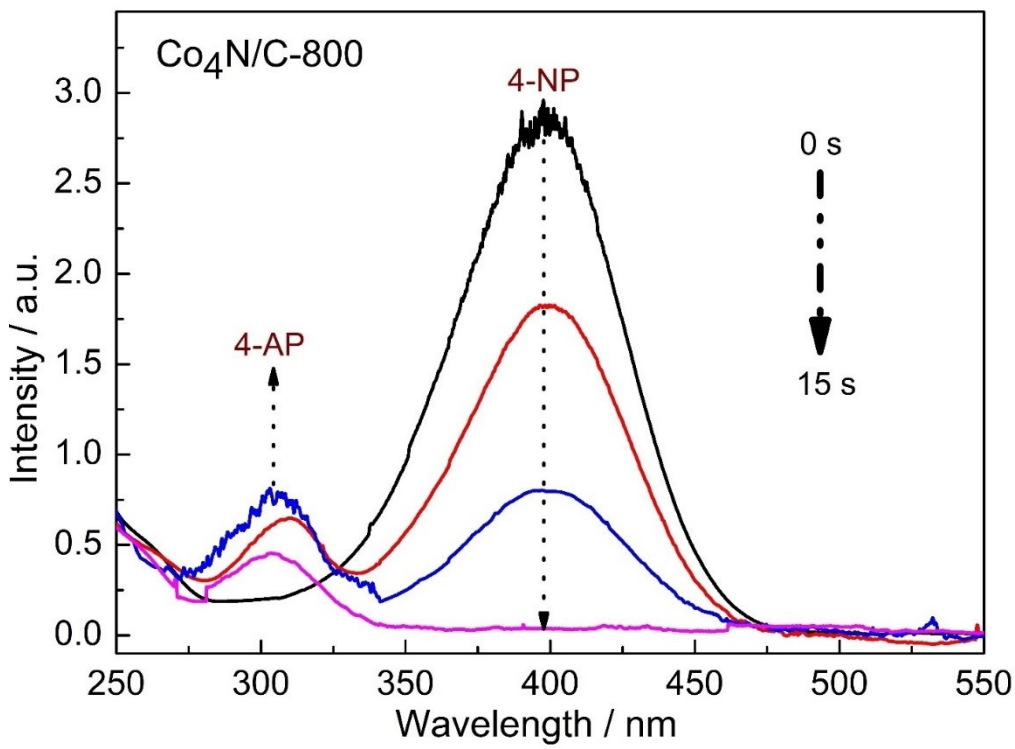

Figure 10. UV-Vis Absorption spectrum of selective reduction of 4-NP in the presence of Co_4N/C-800.

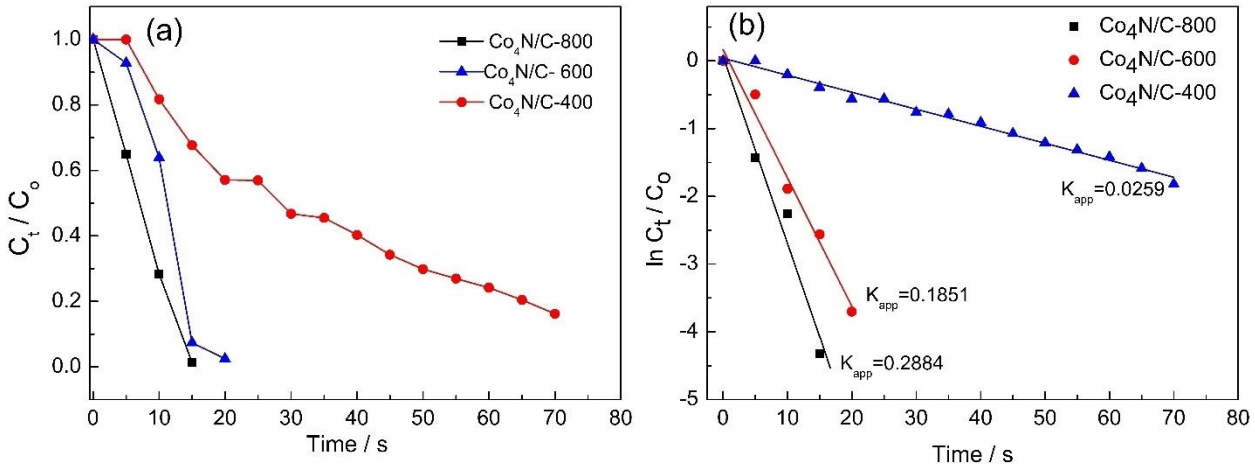

Figure 11. Time-dependent (a) C_t/C_o and (b) ln C_t/C_o plots for the selective conversion of 4-NP in the presence of Co_4N/C-800, Co_4N/C-600, and Co_4N/C-400.

Co_4N/C-800 exhibits superior catalytic activity. Linear relationships of ln C_t/C_o against time, as shown in Figure 11b, confirm the pseudo-first-order kinetics for this reaction. The kinetic constants calculated from the above equation for Co_4N/C-800, Co_4N/C-600 and Co_4N/C-400 are 0.2884 s^{-1}, 0.1851 s^{-1} and 0.0259 s^{-1}, respectively. The coefficient of determination for Co_4N/C-800, Co_4N/C-600 and Co_4N/C-400 is 0.97, 0.96, and 0.99, respectively. The high catalytic activity of Co_4N/C-800 can be attributed to the increased carbonization temperature, which is responsible for faster Co_4N nanoparticle nucleation, resulting in high surface area of Co_4N/C.[57] The polymer phase of cobalt nanocomposite is more profound at lower nitridation temperatures of 400 and 600 °C, demonstrating the absence of C–N architecture, low surface area, and large pore size Co_4N nanoparticle. The reduced surface area and bigger pore size impede the diffusion of 4-NP to the active sites of the catalyst.[57] The apparent rate constants K_{app} calculated for Co (TCNQ)-800 and Co (II)HMTA-800 are 0.05612 s^{-1} and 0.00752 s^{-1}, respectively.

Effect of catalyst loading on 4-NP reduction

Among the various synthesized catalysts, the Co4 N/C-800 catalyst has been further evaluated for the reduction of the 4-NP due to its exceptionally high performance compared to the other synthesized catalysts. The different loadings Co_4N/C-800 catalyst were taken to carry out kinetic studies. The higher the loading amount of Co_4N/C, the higher the number of Co_4N nanoparticles are available, resulting in enhanced catalytic activity.[58] The kinetic studies reveal that the highest loading i.e., 2 mg has the highest kinetic constant and reducing the 4-NP entirely in 15 s. For the catalyst loadings of 1.5 mg, 1 mg, and 0.5 mg, the reduction time was raised to 30 s, 50 s, and 110 s, respectively. The kinetic constants for the catalyst loadings of 2 mg, 1.5 mg, 1 mg, and 0.5 mg are 0.2884 s^{-1}, 0.118 s^{-1}, 0.0708 s^{-1}, and 0.0225 s^{-1}, respectively, which are in good agreement with the fact that increased number of Co_4N nanoparticles for 2 mg loading provided more active sites for the catalytic reduction of 4-NP.

Activation energy (E_a) was calculated from the Arrhenius equation (ln k = ln A − E_a/RT). The Ea was found about 3.038 × 10^{-1} KJ mol^{-1}.

Phenomenal catalytic activity of Co_4N/C-800

The unusual catalytic activity of Co_4N/C-800 can be attributed to its crystallinity, large surface to volume ratio, morphological features as examined by pXRD, SEM, TEM, and BET. Furthermore, the presence of nitrogen over the carbon matrix has been found effective in facilitating the adsorption of 4-NP due to its high positive charge density and weak conjugation, which results in the interaction of the O atom of the OH group nitrophenolate ion to the N-doped species. The increased positive charge density of carbon matrix occurs due to the presence of nitrogen species, resulting in charge delocalization of carbon architecture and absorbing hydrogen ions to catalyze NO_2 group to NH_2 group of 4-AP.[59] The nitrogen-rich environment having valence electrons increases the pi-electron density in the carbon matrix, enhancing the electrical conductivity and surface properties.[60]

Stability and Recyclability of Co_4N/C-800

The stability and recovery of a catalyst need to be determined when industrial applications are considered. The major challenge associated with the catalyst is their recovery after utilization. The synthesized catalyst was found magnetically active, and by applying an external magnetic, the Co_4N/C-800 can be separated from the reaction medium. The already used *p*-nitrophenolate solution was decanted from the beaker, and the catalyst was washed thoroughly with deionized water twice to check the recyclability of the catalyst. The stability of the catalyst was determined by carrying out the reduction process

under a similar set of conditions for five cycles. The catalyst after washing has shown good stability even in the fifth cycle. The first and second cycles of reduction were completed in 25 s and 30s, respectively. For the next third and fourth cycle, the degradation of 4-NP took 45 s to reduce 4-NP to 4-AP completely. The synthesized Co_4N/C-800 catalyst has shown a substantially high catalytic efficiency of 97.57% (Figure 12). The results have demonstrated the catalyst's excellent stability, owing to its crystalline morphology, where Co_4N NPs are encapsulated in carbon support. The presence of nitrogen moieties effectively immobilize the Co_4N Nps, prevented the agglomeration and detaching from the carbon matrix during the recyclability tests, thus improving the catalyst durability.[60]

Dynamic removal and conversion of 4-nitrophenol by sandwiched cellulose membrane filters

In most cases, the static conversion of the 4-nitrophenol into 4-aminophenol has been shown, but the static conversion is not industrial friendly where generally large effluents are produced. There are only a few examples in the literature in which this strategy has been adopted. For continuous conversion of the 4-NP to 4-AP, the catalyst was evenly sandwiched between the two cellulose membrane filters in a vacuum filtration setup (Figure 13). The immediate reduction of the 4-NP into 4-AP has been observed as the 4-NP came in contact with the catalyst immobilized membrane filter and the permeate almost become clear. Furthermore, the appearance of a characteristic peak at 300 nm (4-AP) in the UV-Vis spectrum of the permeate and substantial reduction in the intensity of the peak at 400 nm (4-NP) has confirmed the reduction of hazardous 4-NP to a valorized 4-AP (Table 1 and Figure 14). There is no leaching of catalysts has been observed in the catalytic process. If some catalyst leaches out, it can be magnetically recovered owing to the magnetic nature of cobalt nitride. The continuous practical demonstration of immobilized catalyst on the membrane filter has provided insight to develop a catalyst for the dynamic systems that are more appropriate for the industrial process. Moreover, the catalyst should be controlled through external stimuli such as a magnet to avoid contamination from the catalyst in the water.

Plausible Reaction Mechanism

The reduction of 4-NP to its hydrogenated product by cobalt nitride as catalyst follows Langmuir-Hinshelwood (L-H)

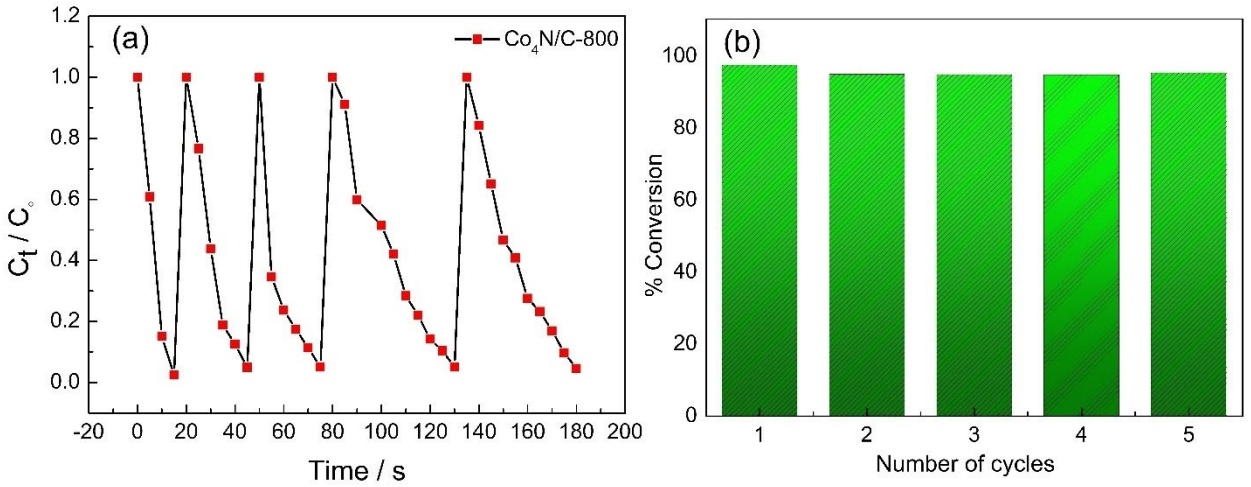

Figure 12. (a) Reusability of Co_4N/C-800 catalyst for the catalytic reduction of 4-NP (b) Catalytic performance of Co_4N/C-800 catalyst in reducing 4-NP to 4-AP for five consecutive cycles.

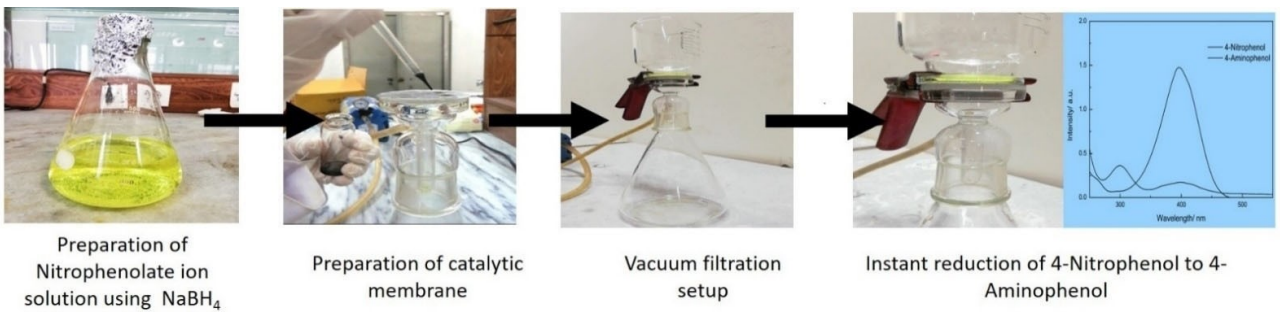

Figure 13. Flowsheet illustration of selective reduction of 4-NP using catalytic membrane setup.

Table 1. Comparative study of several reported catalysts with Co4 N/C-800 for catalytic reduction of 4-NP.

Catalyst	Quantity	Reduction time	TOF	Apparent Rate constant [s^{-1}]	Activation Energy [Ea]	% Conversion	Recyclability cycles	Ref.
Co-NCC	0.27 mg/mL	115 s	-	4.7×10^{-2}	-	100	5	[61]
Au-graphene	1 mg/mL	420 s	-	6.72×10^{-3} s^{-1}	-	93	5	[62]
$SiO_2/Ag_2O@TiO_2$	10 mg	30 s	-	0.17 s^{-1}	-	99.99	4	[63]
Co@CN	5 mg/mL	55 s	-	0.074 s^{-1}	-	95	7	[64]
Co-NB	0.24 g/L	240 s	-	0.0087 s^{-1}	-	96	5	[65]
CoO_x/CN	2 mg	10 min	-	4.2×10^{-3} s^{-1}	-	94.9	8	[66]
Co_4N/NC PNCs	5 mg/mL	1.5 min	52.01×10^{20} molecule $g^{-1}min^{-1}$	2.106 min^{-1}	23.53 KJ mol^{-1}	Drop in efficiency	10	[59]
Rh(0)NPs/Fullerene-C60	0.0025 mg	2 min	2.2 s^{-1}	2.2×10^{-3} s^{-1}	–	100	5	[67]
Au/MCN	20 mg	15 min	13.7 min^{-1}	0.34 min^{-1}	–	100	15	[68]
Pt-NP/TiO_2-PAN NF	2 mg	45 s	4.44 s^{-1}	0.1102 s^{-1}	–	100	8	[69]
Cu/rGO	7.44×10^{-3} mg/3 mL	180 s	298.7×10^{-6} mmol $mg^{-1}s^{-1}$	23.2×10^{-3} s^{-1}	–	92	10	[70]
Asparagine chitosan NPs	25 mg	6 min	–	0.4861 min^{-1}	24.03 KJ mol^{-1}	–	3	[71]
Co_4N/C-800	2 mg/mL	15 s	3.5 s^{-1*}	0.2884 s^{-1}	3.038×10^{-1} KJ mol^{-1}	97.57	5	This study

*Turnover frequency (TOF) = [Moles of 4-AP Yield]/[(Moles of Co loading) × (Reaction time) × Dispersion/Molar weight of Co].[72]

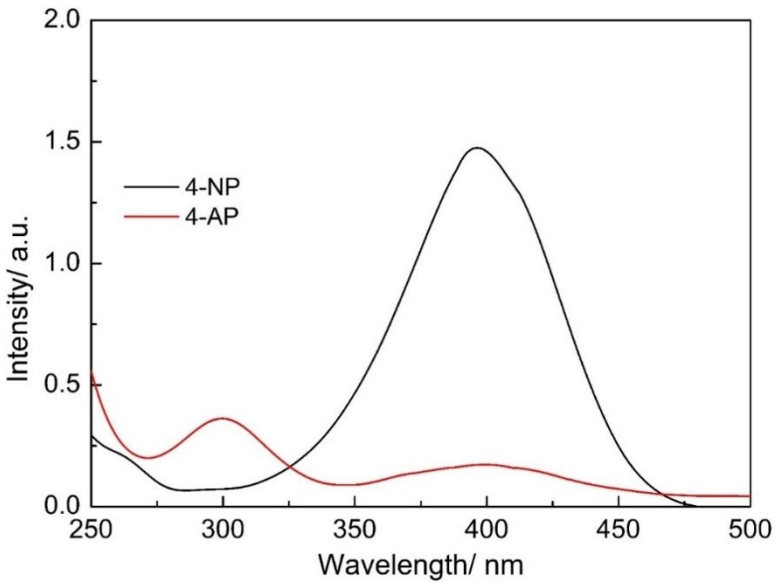

Figure 14. UV spectrum of 4-NP and 4-AP obtained from membrane setup.

mechanism[73] as presented in Figure 15. Getting an insight into the reaction process shows that $NaBH_4$ initially hydrolyzes to BH_4^- to give electrons and liberates hydrogen species on the surface of the carbon matrix. Subsequently, the chemisorption of 4-NP onto carbon support occurs, causing the electrons and hydrogen species liberated from $NaBH_4$ to be carried to the nitrogen of the nitro group of 4-NP to the carbon support. It can be observed that both reactants are adsorbed to the surface of the catalyst prior to the reaction, following the L-H mechanism.[74] A transition surface complex of 4-hydroxyl aminophenol is formed due to the transfer of electrons and active H species. Loss of H_2O molecule from this transition state converts into 4-AP. It is worth noting that the surface of Co_4N/C connects the two adsorbates via electrons and H^+ species to transfer the electrons from the oxidation to the reduction site.[61] Lastly, the desorption of 4-AP occurs from the catalyst surface to provide an active site for the next reduction cycle.

3. Conclusion

In summary, we have demonstrated the successful synthesis of a highly potent nano-catalyst Co_4N/C by direct carbonization of coordination polymer containing nitrogen-rich ligands under N_2 flow at 400, 600, and 800 °C. Annealing temperature has shown a significant impact on the properties of the synthesized

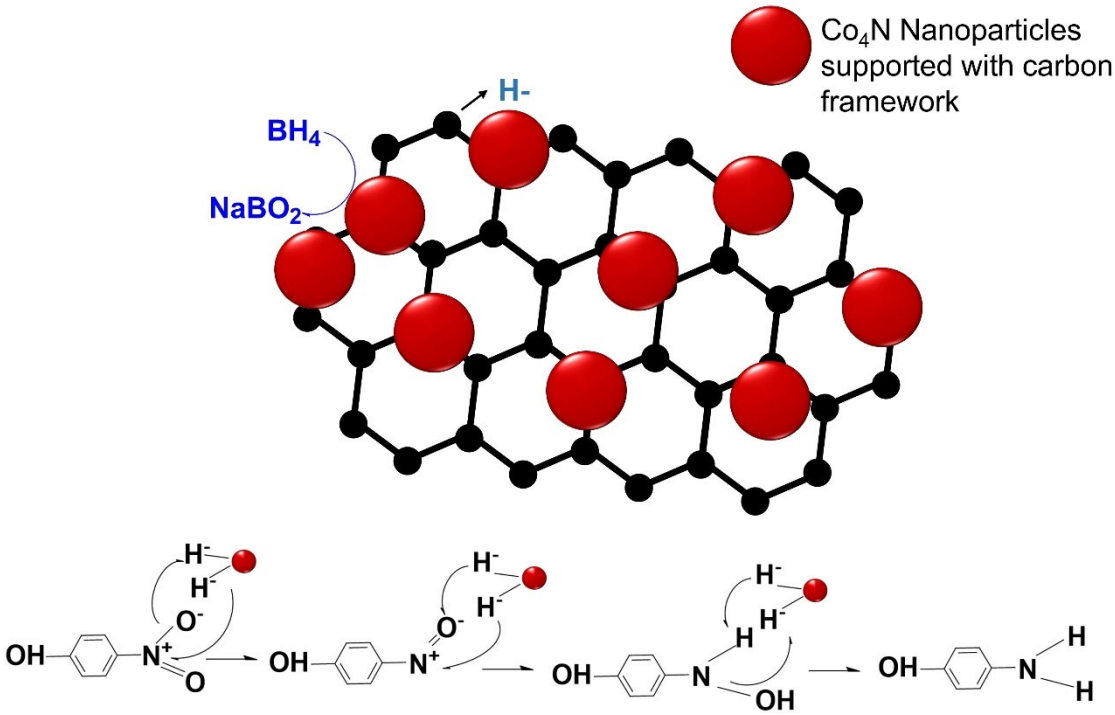

Figure 15. Schematic illustration of the catalytic reduction of 4-NP to 4-AP on Co_4N/C-800 nanostructures.

nanoparticles. The nanostructured catalyst Co_4N/C-800, among other synthesized catalysts, has shown outstanding catalytic activity for the reduction of the 4-NP to 4-AP within a very short time (15 s). Furthermore, the catalyst is magnetically active and recollected from the aqueous medium with the external stimuli of the magnet. The developed catalyst was used for the successive five cycles, and it has remained stable. The catalyst has been evaluated for the continuous conversion of the 4-NP to 4-AP by immobilizing on the surface of the cellulose membrane filter. The immobilized catalyst has shown excellent performance for the dynamic conversion of the 4-NP to 4-AP and 4-NP in the contaminated water, immediately reduced. The conversion efficiency of the nanostructured Co_4N/C-800 catalyst was found relatively high, i.e., ~97.57%. This study presents a simplistic approach for the synthesis of Co_4N/C catalysts and also provides a practical demonstration as a heterogeneous catalyst for reducing nitroarenes to hydrogenated products. It also provides an insight into the development of the catalytic membranes for the continuous conversion or removal of toxic contaminants from the water.

4. Materials and Methods

Synthesis of Coordination Polymer

The coordination polymer was synthesized using a simple, cost-effective, and scalable approach. $TCNQH_2$ (7, 7, 8, 8-tetracyanoquinodimethane) (2.4 mmol, 500 mg) was added into 50 mL ethanol and kept at 45 °C with stirring for 30 min. Subsequently to this solution, triethylamine (4.8 mmol, 48.57 mg) dissolved in 10 mL ethanol was added to form solution I. Hexamethyltetraamine (HMTA) (4.8 mmol, 1368 mg) dissolved in 50 mL ethanol was sonicated for 20 minutes. For metal precursor, $CoCl_2 \cdot 6H_2O$ (2.4 mmol, 31.16 mg) in 50 mL of ethanol was kept at 45 °C with continuous stirring for 10 min, resulting in a clear dark blue solution. To the HMTA solution, $CoCl_2 \cdot 6H_2O$ solution was added dropwise with gentle heating at 45 °C under continuous stirring, resulting in the formation of solution II. The precursor solution I was heated to reach the boiling point of ethanol, i.e., 79 °C by reflux, in a round bottom flask placed in an oil bath for 30 min. The mixture was cool for 30 min followed by the introduction of solution II. The two precursor solutions were then refluxed for 24 h. A brownish-black murky solution mixture was obtained, vacuum filtered, and then thoroughly washed with ethanol followed by acetonitrile until the filtrate becomes clear. The as-obtained product was vacuum dried at 50 °C for 12 h. The process as mentioned above has been illustrated in Scheme 1.

Synthesis of Co_4N/C-400 -600, and -800

The as-synthesized cobalt coordination polymer was annealed at different temperatures under N_2 flow. The process was carried out in a tube furnace under stable, inert conditions. The Co coordination polymer was placed in a porcelain boat, and the temperature was raised to 400, 600 and 800 °C for different batches of coordination polymer to form Co_4N/C-400, Co_4N/C-600, and Co_4N/C-800, respectively. A 10 °C per min temperature

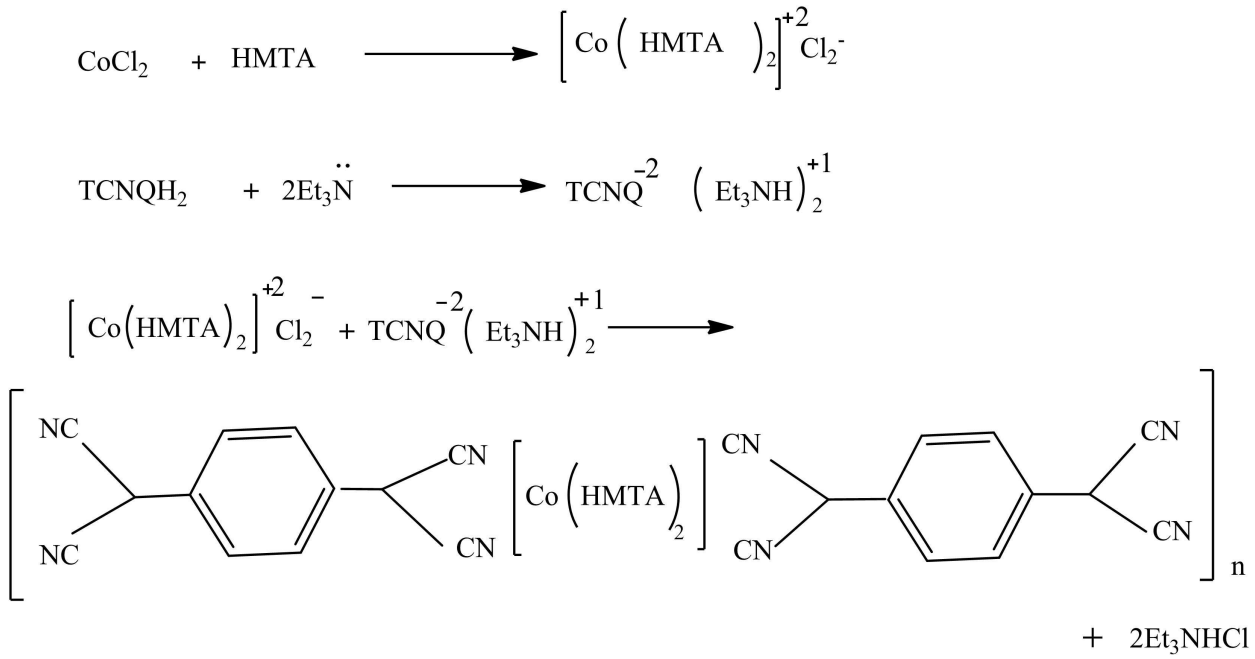

Scheme 1. Schematic representation of chemical reactions involved in the synthesis of Cobalt nitride precursor.

rise was employed to reach the respective annealing temperature. On completion of the nitridation process, the reactor was slowly cooled down to room temperature under N_2 flow.

Synthesis of [Co (TCNQ]Cl_2 complex

A coordination complex of Co and TCNQ was synthesized for the comparison of catalytic activity. TCNQ (1.2 mmol, 250 mg) dissolved in 20 mL ethanol was heated with constant stirring at 45 °C followed by the introduction of trimethylamine (2.4 mmol, 350 µL) dissolved in 10 mL ethanol. Subsequently, $CoCl_2 \cdot 6H_2O$ (2.4 mmol, 103.87 mg) dissolved in 20 mL ethanol in a glass container was added to the previously prepared solution. This solution was refluxed for 5 h and then washed with ethanol and acetonitrile and vacuum dried at 50 °C for 10 h. This as-synthesized complex was further annealed in a tube furnace at 800 °C under constant N_2 flow, which is labelled as Co(TCNQ)-800.

Synthesis of Co (II)-HMTA complex

Co (II)-HMTA complex was synthesized based on reported method.[38] HMTA (0.195 mol, 2.73 g) dissolved in 30 mL ethanol was sonicated with slight heating and then magnetically stirred. Then $CoCl_2 \cdot 6H_2O$ (2.4 mmol, 0.3168 g) dissolved in 20 mL ethanol was subjected to HMTA solution. The mixture was left to stir for 3 h. The product was obtained in the form of pink precipitates, which were vacuum filtered and washed and dried at 50 °C for 5 h in a vacuum oven. The obtained complex was subjected to annealing in a tube furnace at 800 °C while keeping N_2 flow constant. The obtained product was named Co(II)HMTA-800 for further discussion.

Catalytic reduction of 4-Nitrophenol

The catalytic activity of the synthesized nanocomposites was evaluated against a well-known model reaction to selectively reduce the 4-Nitrophenol (4-NP) to 4-Aminophenol (4-AP) in the presence of sodium borohydride ($NaBH_4$). The catalytic runs were observed by UV-Vis spectroscopy. Nitrophenol solution (0.3 mM, 10.4 mg) was prepared in a volumetric flask in deionized water (250 mL). Subsequently, excess $NaBH_4$ (1 M, 1.89 g) dissolved in deionized water (50 mL) was added to the 4-NP solution, and the color of the solution immediately turned bright yellow from pale yellow. This solution was poured into a 3 mL quartz cell, followed by adding different amounts of composites for different catalytic runs. The synthesized catalysts (Co4 N/C) were magnetically active; the used catalysts in the reaction system were collected magnetically and washed three times with deionized water to analyze their reusability and recyclability.

Characterization

FTIR spectra of coordination polymer were recorded for structural analysis by between 500 and 4000 cm^{-1} with a ATR-FTIR Alpha II, Bruker Scientific LLC (Billerica, MA 01821, USA). Crystalline phases of resulting nitrides were characterized by powder X-ray powder diffraction (pXRD) profiles using a Bourevestnik Dron-8, (Saint-Petersburg 190900, Russia) instru-

ment with a Cu Kα (λ = 1.5418 Å) X-ray source, a step size of 0.05, and exposure time 5°/min. X-ray photoelectron spectroscopy (XPS) was carried out with ESCALAB 250Xi, Thermo Scientific, UK instrument using AlKα radiation, to evaluate prepared catalysts' electronic and chemical states. Further chemical bonding states and graphitization process was illustrated through Raman Spectroscopy using a Renishaw in Via™Reflex micro spectrometer (Gloucestershire, United Kingdom, GL12 8JR) with a 532 nm laser excitation. Nitrogen adsorption and desorption isotherms for determining surface area and porosity were recorded on micromeritics Gemini VII 2390 surface analyzer (PA-18936 Montgomeryville, United States). The samples were degassed before the adsorption experiment at 500 °C for 5 h, and the p/p° was kept within the range of 0.05-1 (Sample degas system: micromeritics Vac Prep061). The Brunauer Emmett Teller (BET) was used to calculate specific surface area, and pore volume was measured from the adsorbed amount at p/p° 0.05-1. Scanning electron microscopy (SEM), elemental mapping and energy dispersive surface (EDS) analysis were carried out with a Nova NanoSEM instrument (Hillsboro, Oregon 97123, US) and transmission electron microscope of JEOL 2100 F (Joel USA Inc Peabody, MA 01960, USA) was used for studying high-resolution morphology and inter-planar distances. The thermal decomposition rate of coordination polymer was determined by TGA 5500 Discovery instrument (Thermal Analysis Company, TA Instruments, New Castle, DE 19720, USA) under an inert atmosphere. X-ray photoelectron spectroscopy was carried out utilizing the Thermos Scientific (Waltham, MA USA 02451) Escalab 250Xi spectrometer fitted with Al Kα (1486.6 eV) X-ray source. The X-ray absorption fine structure (XAFS) spectra were measured on the XAFS/XRF beamline, Synchrotron-Light for Experimental Science and Applications in the Middle East (SESAME), operating at 2.5 GeV in "decay" mode with a maximum electron current of 250 mA. XAFS spectra were acquired in fluorescence mode with a Silicon Drift Detectors (SDD), KETEK GmbH at room temperature, in the spectral range of Co K-edge (7709 eV) for the Co_4N thin film. X-ray beam intensity before and after the sample was also measured by two ionization chambers filled with a mixture of noble gases and XAFS data were acquired with a double-crystal Si (220) monochromator. The energy was calibrated according to the absorption *K*-edge of Co metallic foil. The already prepared Co_4N thin film was directly used for XAFS data measurement.

The absorbance of nitrophenolate ion solution was recorded on a UV-Vis Spectrophotometer, UV-1700 Pharma Spec Shimadzu (Santa Clara, CA 95051, United States), equipped with a quartz cuvette.

Associated Content

Supporting Information: pXRD of pristine [Co (TCNQ)] Cl_2] and [Co (TCNQ)] Cl_2] annealed at 800 °C, pXRD of pristine Co (II) HMTA and Co (II) HMTA annealed at 800 °. Absorption spectra of 4-Nitrophenol before and after the addition of $NaBH_4$. Absorption spectra of nitrophenolate ions without the addition of catalyst. UV-Vis Absorption spectrum of selective reduction of 4-NP in the presence of Co_4N/C-600 and Co_4N/C-400 in (a) and (b), respectively. UV-Vis absorption spectra of catalyst loadings of (a) 1.5 mg (b) 1 mg and (c) 0.5 mg of Co_4N/C-800. UV-Vis absorption spectra of selective reduction of 4-NP in the presence of (a) Co(TCNQ)-800 and (b) Co(II) HMTA-800. Time dependent (a) C_t/C_o and (b) ln C_t/C_o plots for the selective conversion of 4-NP with different catalyst loadings of Co_4N/C-800. Activation energy by Arrhenius plot for Co_4N/C-800.

Acknowledgements

We also extend gratitude to the XAFS/XRF beamline, SESAME, for the XAFS spectra measurements (proposal No. 20185131). Open Access funding enabled and organized by Projekt DEAL.

Conflict of Interest

The authors declare no conflict of interest.

Data Availability Statement

Data sharing is not applicable to this article as no new data were created or analyzed in this study.

Keywords: catalytic membranes · cobalt nitride · nano-catalyst · selective reduction · tetracyanoquinodimethane

[1] F. Lévy, P. Hones, P. E. Schmid, R. Sanjinés, M. Diserens, C. Wiemer, *Surf. Coat. Technol.* **1999**, *120–121*, 284–290.
[2] C. Stampfl, W. Mannstadt, R. Asahi, A. J. Freeman, *Phys. Rev. B* **2001**, *63*, 155106.
[3] X. Tian, J. Luo, H. Nan, Z. Fu, J. Zeng, S. Liao, *J. Mater. Chem. A* **2015**, *3*, 16801–16809.
[4] W. Sun, A. Holder, B. Orvañanos, E. Arca, A. Zakutayev, S. Lany, G. Ceder, *Chem. Mater.* **2017**, *29*, 6936–6946.
[5] R. S. Ningthoujam, N. S. Gajbhiye, *Prog. Mater. Sci.* **2015**, *70*, 50–154.
[6] a) A. Fischer, J. O. Müller, M. Antonietti, A. Thomas, *ACS Nano* **2008**, *2*, 2489–2496; b) E. Gregoryanz, C. Sanloup, M. Somayazulu, J. Badro, G. Fiquet, H.-k. Mao, R. J. Hemley, *Nat. Mater.* **2004**, *3*, 294–297.
[7] R. Marchand, F. Tessier, F. J. DiSalvo, *J. Mater. Chem.* **1999**, *9*, 297–304.
[8] X. Liu, W. Zang, C. Guan, L. Zhang, Y. Qian, A. M. Elshahawy, D. Zhao, S. J. Pennycook, J. Wang, *ACS Energy Lett.* **2018**, *3*, 2462–2469.
[9] R. d. Paiva, R. A. Nogueira, J. L. A. Alves, *Braz. J. Phys.* **2006**, *36*, 470–473.
[10] D. R. Glasson, S. A. A. Jayaweera, *J. Appl. Chem.* **1968**, *18*, 65–77.
[11] a) E. Z. Lee, Y. S. Jun, W. H. Hong, A. Thomas, M. M. Jin, *Angew. Chem.* **2010**, *122*, 9900–9904; *Angew. Chem. Int. Ed.* **2010**, *49*, 9706–9710; b) F. Xie, X. Cao, F. Qu, A. M. Asiri, X. Sun, *Sens. Actuators* **2018**, *255*, 1254–1261.
[12] N. Pandey, M. Gupta, R. Gupta, Z. Hussain, V. R. Reddy, D. M. Phase, J. Stahn, *Phys. Rev. B* **2019**, *99*, 214109.
[13] B. Mazumder, A. L. Hector, *J. Mater. Chem.* **2009**, *19*, 4673–4686.
[14] a) M. Yang, R. Guarecuco, F. J. DiSalvo, *Chem. Mater.* **2013**, *25*, 1783–1787; b) C. Giordano, M. Antonietti, *Nano Today* **2011**, *6*, 366–380.
[15] S. Dong, X. Chen, X. Zhang, G. Cui, *Coord. Chem. Rev.* **2013**, *257*, 1946–1956.
[16] A.-M. Alexander, J. S. J. Hargreaves, *Chem. Soc. Rev.* **2010**, *39*, 4388–4401.
[17] a) S. T. Oyama, *Catal. Today* **1992**, *15*, 179–200; b) A. B. Dongil, *Nanomaterials* **2019**, *9*, 1111.

[18] S. T. Oyama, in *The chemistry of transition metal carbides and nitrides*, Springer, **1996**, pp. 1–27.
[19] P. Afanasiev, *Inorg. Chem.* **2002**, *41*, 5317–5319.
[20] M. K. Neylon, S. Choi, H. Kwon, K. E. Curry, L. T. Thompson, *Appl. Catal. A* **1999**, *183*, 253–263.
[21] a) J. S. J. Hargreaves, *Appl. Petrochem. Res.* **2014**, *4*, 3–10; b) C. J. H. Jacobsen, *Chem. Commun.* **2000**, 1057–1058.
[22] a) L. Yu, Q. Zhu, S. Song, B. McElhenny, D. Wang, C. Wu, Z. Qin, J. Bao, Y. Yu, S. Chen, Z. Ren, *Nat. Commun.* **2019**, *10*, 5106; b) J. Theerthagiri, S. J. Lee, A. P. Murthy, J. Madhavan, M. Y. Choi, *Curr. Opin. Solid State Mater. Sci.* **2020**, *24*, 100805.
[23] K. Xu, P. Chen, X. Li, Y. Tong, H. Ding, X. Wu, W. Chu, Z. Peng, C. Wu, Y. Xie, *J. Am. Chem. Soc.* **2015**, *137*, 4119–4125.
[24] P. Chen, K. Xu, Z. Fang, Y. Tong, J. Wu, X. Lu, X. Peng, H. Ding, C. Wu, Y. Xie, *Angew. Chem.* **2015**, *127*, 14923–14927; *Angew. Chem. Int. Ed.* **2015**, *54*, 14710–14714.
[25] N. Han, P. Liu, J. Jiang, L. Ai, Z. Shao, S. Liu, *J. Mater. Chem. A* **2018**, *6*, 19912–19933.
[26] A. Fischer, M. Antonietti, A. Thomas, *Adv. Mater.* **2007**, *19*, 264–267.
[27] Y. Xie, Y. Qian, W. Wang, S. Zhang, Y. Zhang, *Science* **1996**, *272*, 1926–1927.
[28] G. M. Brown, L. Maya, *J. Am. Ceram. Soc.* **1988**, *71*, 78–82.
[29] K. Niwa, T. Terabe, D. Kato, S. Takayama, M. Kato, K. Soda, M. Hasegawa, *Inorg. Chem.* **2017**, *56*, 6410–6418.
[30] L. Oar-Arteta, T. Wezendonk, X. Sun, F. Kapteijn, J. Gascon, *Mater. Chem. Front.* **2017**, *1*, 1709–1745.
[31] K. Murugesan, V. G. Chandrashekhar, T. Senthamarai, R. V. Jagadeesh, M. Beller, *Nat. Protoc.* **2020**, *15*, 1313–1337.
[32] I. Asif, N. Baig, M. Sher, A. Ul-Hamid, M. Altaf, A. Mumtaz, M. Sohail, *Clean. Eng. Technol.* **2021**, *2*, 100081.
[33] T. A. Hudson, R. Robson, *Cryst. Growth Des.* **2009**, *9*, 1658–1662.
[34] K. Medjanik, S. Perkert, S. Naghavi, M. Rudloff, V. Solovyeva, D. Chercka, M. Huth, S. A. Nepijko, T. Methfessel, C. Felser, M. Baumgarten, K. Müllen, H. J. Elmers, G. Schönhense, *Phys. Rev. B* **2010**, *82*, 245419.
[35] a) F. Hoshyargar, A. P. O'Mullane, *ChemCatChem* **2016**, *8*, 2335–2339; b) M. Mahajan, S. K. Bhargava, A. P. O'Mullane, *RSC Adv.* **2013**, *3*, 4440–4446.
[36] L. Fu, Y. Chen, S. Zhao, Z. Liu, R. Zhu, *RSC Adv.* **2016**, *6*, 19482–19491.
[37] X. Zhuang, W. Zhao, F. Zhang, Y. Cao, F. Liu, S. Bi, X. Feng, *Polym. Chem.* **2016**, *7*, 4176–4181.
[38] C. D. Tabong, A. M. Ondoh, D. M. Yufanyi, J. Foba, *J. Mater. Sci. Res.* **2015**, *4*, 70.
[39] D. A. Pyles, J. W. Crowe, L. A. Baldwin, P. L. McGrier, *ACS Macro Lett.* **2016**, *5*, 1055–1058.
[40] L. Bokobza, J.-L. Bruneel, M. Couzi, *J. Carbon Res.* **2015**, *1*, 77–94.
[41] T. Liu, M. Li, L. Guo, *Talanta* **2018**, *181*, 154–164.
[42] P. Chen, K. Xu, Y. Tong, X. Li, S. Tao, Z. Fang, W. Chu, X. Wu, C. Wu, *Inorg. Chem. Front.* **2016**, *3*, 236–242.
[43] F. Meng, H. Zhong, D. Bao, J. Yan, X. Zhang, *J. Am. Chem. Soc.* **2016**, *138*, 10226–10231.
[44] G. Prieto, A. Martínez, R. Murciano, M. A. Arribas, *Appl. Catal. A* **2009**, *367*, 146–156.
[45] M. Chen, L. L. Shao, Z. M. Gao, T. Z. Ren, Z. Y. Yuan, *J. Power Sources* **2015**, *286*, 82–90.
[46] H. B. Bhandari, J. Yang, H. Kim, Y. Lin, R. G. Gordon, Q. M. Wang, J.-S. M. Lehn, H. Li, D. Shenai, *ECS J. Solid State Sci. Technol.* **2012**, *1*, N79.
[47] R. N. Panda, S. B. Dalavi, J. Theerthagiri, *Adsorpt. Sci. Technol.* **2012**, *30*, 345–354.
[48] a) K. Murugesan, T. Senthamarai, M. Sohail, A. S. Alshammari, M.-M. Pohl, M. Beller, R. V. Jagadeesh, *Chem. Sci.* **2018**, *9*, 8553–8560; b) L. Tan, B. Tan, *Chem. Eng. J.* **2020**, *390*, 124485.
[49] B. Chang, Y. Zhong, Z. Ai, J. Zhang, D. Shi, K. Zhang, Y. Shao, J. Shen, B. Huang, L. Zhang, Y. Wu, X. Hao, *New J. Chem.* **2019**, *43*, 14701–14707.
[50] W. D. L. Cruz, O. E. Contreras, G. Soto, E. J. R. M. D. F. Pérez-Tijerina, *Rev. Mex. Fis.* **2006**, *52*, 409–412.
[51] P. Lazar, R. Mach, M. Otyepka, *J. Phys. Chem. C* **2019**, *123*, 10695–10702.
[52] R. Yadav, C. K. Dixit, *J. Sci. Adv. Mater. Devices* **2017**, *2*, 141–149.
[53] M. Muoz, F. Farges, P. Argoul, *Phys. Scr.* **2005**, *T115*, 221–222.
[54] L. U. Khan, N. Jabeen, I. Jabbar, S. Jamil, A. Kanwal, Z. Akhter, M. Usman, M. Z. Abid, M. Harfouche, *ACS Appl. Mater. Interfaces* **2021**, *4*, 2049–2055.
[55] X.-k. Kong, Z.-y. Sun, M. Chen, C.-l. Chen, Q.-w. Chen, *Energy Environ. Sci.* **2013**, *6*, 3260–3266.
[56] R. Cai, P. R. Ellis, J. Yin, J. Liu, C. M. Brown, R. Griffin, G. Chang, D. Yang, J. Ren, K. Cooke, P. T. Bishop, W. Theis, R. E. Palmer, *Small* **2018**, *14*, e1703734.
[57] Y. Yusran, D. Xu, Q. Fang, D. Zhang, S. Qiu, *Microporous Mesoporous Mater.* **2017**, *241*, 346–354.
[58] Y. Hao, X. Shao, B. Li, L. Hu, T. Wang, *Mater. Sci. Semicond. Process.* **2015**, *40*, 621–630.
[59] J. Sheng, L. Wang, L. Deng, M. Zhang, H. He, K. Zeng, F. Tang, Y.-N. Liu, *ACS Appl. Mater. Interfaces* **2018**, *10*, 7191–7200.
[60] Y. Tian, Y.-y. Cao, F. Pang, G.-q. Chen, X. Zhang, *RSC Adv.* **2014**, *4*, 43204–43211.
[61] Z. Hasan, D.-W. Cho, C.-M. Chon, K. Yoon, H. Song, *Chem. Eng. J.* **2016**, *298*, 183–190.
[62] S. Li, S. Guo, H. Yang, G. Gou, R. Ren, J. Li, Z. Dong, J. Jin, J. Ma, *J. Hazard. Mater.* **2014**, *270*, 11–17.
[63] O. A. Zelekew, D.-H. Kuo, *Phys. Chem. Chem. Phys.* **2016**, *18*, 4405–4414.
[64] S.-T. Li, G.-M. Shi, J.-S. Liang, X.-L. Dong, F.-N. Shi, L.-M. Yang, S.-H. Lv, *Nanotechnology* **2019**, *31*, 065701.
[65] D.-W. Cho, K.-H. Jeong, S. Kim, D. C. Tsang, Y. S. Ok, H. Song, *Sci. Total Environ.* **2018**, *612*, 103–110.
[66] X. Zhang, N. Wang, L. Geng, J. Fu, H. Hu, D. Zhang, B. Zhu, J. Carozza, H. Han, *J. Colloid Interface Sci.* **2018**, *512*, 844–852.
[67] M. Gopiraman, S. Saravanamoorthy, S. Ullah, A. Ilangovan, I. S. Kim, I. M. Chung, *RSC Adv.* **2020**, *10*, 2545–2559.
[68] S. Chen, H. Fu, L. Zhang, Y. Wan, *Appl. Catal. B* **2019**, *248*, 22–30.
[69] A. Celebioglu, K. S. Ranjith, H. Eren, N. Biyikli, T. Uyar, *Sci. Rep.* **2017**, *7*, 13401.
[70] X. Kang, D. Teng, S. Wu, Z. Tian, J. Liu, P. Li, Y. Ma, C. Liang, *J. Colloid Interface Sci.* **2020**, *566*, 265–270.
[71] M. Saxena, R. Saxena, *Mater. Chem. Phys.* **2022**, *276*, 125437.
[72] X. Tian, M. Zahid, W. Sun, Y. Zhu, *Appl. Surf. Sci.* **2021**, *566*, 150615.
[73] S. R. Thawarkar, B. Thombare, B. S. Munde, N. D. Khupse, *RSC Adv.* **2018**, *8*, 38384–38390.
[74] M. Du, Q. Liu, C. Huang, X. Qiu, *RSC Adv.* **2017**, *7*, 35451–35459.

Manuscript received: October 29, 2021
Revised manuscript received: December 30, 2021
Accepted manuscript online: January 3, 2022
Version of record online: January 19, 2022